12-2018

Effect of Strain Rate on the Tensile Behavior of CoCrFeNi and CoCrFeMnNi High Entropy Alloys

Mitra Shabanisamghabady
Clemson University, mitra.shabani1991@gmail.com

Follow this and additional works at: https://tigerprints.clemson.edu/all_theses

EFFECT OF STRAIN RATE ON THE TENSILE BEHAVIOR OF CoCrFeNi AND
CoCrFeMnNi HIGH ENTROPY ALLOYS

A Thesis
Presented to
the Graduate School of
Clemson University

In Partial Fulfillment
of the Requirements for the Degree
Master of Science
Mechanical Engineering

by
Mitra Shabanisamghabady
December 2018

Accepted by:
Dr. Garrett J. Pataky: Thesis Advisor, Committee Chair
Dr. Huijuan Zhao
Dr. Gang Li

Abstract

High entropy alloys (HEAs) are a new class of alloys with the potential to be used in critical load bearing applications instead of conventional alloys. The HEAs studied in this research were CoCrFeNi and CoCrFeMnNi. Both were single-phase face-centered cubic materials. The focus of this study was on the tensile behavior of the two materials at quasi-static and dynamic strain- rates (10^{-4} to 10^{3} s^{-1}) and the underlying microstructural phenomena driving the behaviors. Electron back-scatter diffraction was performed on both HEAs to study the microstructure before mechanical testing. To study the effect of strain rate, tensile experiments were performed at quasi-static strain rates on hydraulic MTS load frames and dynamic strain-rates on a Split- Hopkinson Pressure Bar. HEAs stress-strain curves, modulus of elasticity, yield strength, ultimate strength, strain-rate sensitivity and work hardening rates were calculated with the data from the tensile experiments. Transmission electron microscopy was performed post-mortem to study the plastic deformation mechanisms activated at different strain rates.

The dominant deformation mechanism changed from dislocation slip at quasi-static strain-rates to the addition of deformation nano-twins at dynamic strain-rates. Ultimate strength and ductility both improved with the increase of strain-rate, which can be attributed to the activation of deformation nano-twins in HEAs. CoCrFeNi and CoCrFeMnNi both have low stacking fault energies which encouraged twinning at high strains to accommodate plastic deformation. The strain-rate sensitivity component increased with increasing strain-rate, beginning with negligible strain-rate sensitivity in the quasi-static range to high strain-rate sensitivity in the dynamic range. CoCrFeMnNi showed greater strain-rate sensitivity. CoCrFeNi, with the less configurational entropy, had higher

mechanical properties and strain hardening rates at different strain-rates compared to CoCrFeMnNi.

Acknowledgements

I would like to first thank my advisor, Dr. Garrett J. Pataky, for his support, patience, and encouragement throughout my master's studies. His knowledge and guidance were essential to the completion of this thesis. I have been very lucky to join his research group and work under his supervision. He is very thoughtful and provided resources necessary for developing research and academic skills aligned with my goal of joining the academia.

I would like to thank Dr. Huijuan Jane Zhao and Dr. Gang Li for agreeing to be on my committee and meeting with me throughout my time here to discuss my research.

I would like to thank my family for their love, support and motivation. I would not have been able to come this far without their endless support. They have always encouraged me to pursue education and they have been my role models in all aspects of life. I would like to thank my sister for always being there for me to talk and share ideas.

I would like to thank the Clemson University, the Clemson Mechanical Engineering Department, all of my professors, all of the welcoming people and all of the friends I have made during my time here. I would especially like to thank my office mates of EIB 125, who became my great friends since joining this research group: Cameron Abarotin, Jody Bartanus, Jacob Biddlecom, Kaitlynn Conway and Matt Williams.

I would like to thank Dr. Kavan Hazeli and Joseph Indeck from the University of Alabama

in Huntsville for their collaboration on this research.

I would also like to thank Clemson University Advanced Materials Research Lab (AMRL) personnel for helping me when using the facility for this research.

Table of Contents

List of Figures

List of Figures (Continued)

List of Tables

Chapter 1. Introduction

1.1 Literature Review

1.1.1   High Entropy Alloys

For thousands of years conventional alloying strategies have been used. Conventional alloying strategy is to select one major component based on the main property that is expected from the material and then adding alloying additions. For instance, copper has a good electrical conductivity, but it is very soft and therefore Beryllium is added as the secondary property to add strength. High entropy alloys (HEAs) are metal alloys that are based on multiple components rather than one or two which is the case for conventional alloys. Using conventional alloying strategies limits the different kinds of alloys that can be achieved. HEAs or multicomponent alloys were first proposed by Yeh et al. and Cantor et al. in 2004 [1–5]. Cantor started working on systems of alloys with multiple principle elements in equi-molar or close to equi-molar proportions with the idea of not limiting the different alloys that can be made as a result of following the conventional alloying strategies. The multi-element alloying strategy is to mix large number of components in equal or near-equal proportions. Using this strategy, more alloys can be made possibly resulting to alloys with desired properties. To understand the limitation that using the conventional alloying strategy is causing at least in the number of the possible alloys, system with C components can be considered. Distinction between the composition can be considered to be x% therefore it can be said that there is n=100/x composition for each component. The total number of alloys is then:

$$N = \frac{(C+n-1)!}{(c-1)!n!} \tag{1}$$

Considering C to be 60 (from the 120 known elements) and x being 0.1 then the total number of possible alloys would be around 10^{100}. This can be compared to the conventional binaries and ternaries being around 10^{11} [5]. Therefore, lots of possibilities are rising using the multi-component alloying method which need to be further studied.

Knowledge on the behavior of pure materials and the conventional alloys are fairly vast whereas how the materials resulting from mixing multiple elements in equi-molar proportions is being studied only recently and therefore more studies need to be done.

Yeh introduced the same idea that Cantor had of multi-component alloys, but he introduced them as high entropy alloys. The alloys are made up of multiple number of elements in equi-molar or near equi-molar values and this increases disorder in the system and therefor the entropies of these alloys are high. The configurational entropy change per mole can be found following Boltzmann's hypothesis resulting in the equation 2:

$$\Delta S_{conf} = R \ln n \tag{2}$$

where, n is the number of elements in the system with equimolar fractions and R is the gas constant. This in turn results in low Gibb's free energy of formation (equation 3) considering that the enthalpy of formation of binary compounds and systems with more number of elements are within the same range [4]:

$$\Delta G = \Delta H_{conf} - T\Delta S_{conf} \tag{3}$$

Where, ΔG is the Gibb's free energy of formation, ΔH_{conf} is the enthalpy of formation, T is the temperature and ΔS_{conf} is the formation entropy increase of the system. Based on this Yeh's idea was that this low Gibb's energy resulting from the high entropy of formation in high entropy alloys is responsible for the formation of random solid solution during solidification rather than the formation of intermetallic compounds.

HEAs were introduced having four core effects: (1) Entropic phase stabilization, (2) severe lattice distortion, (3) sluggish diffusion and (4) cocktail effect. But recently these four effects and their contribution to the HEA improved material properties have been challenged [6, 7]. HEAs have different types based on their main components. Different types of HEAs can be seen in Figure 1.

The principle components in HEA usually are in equi-molar or near equi-molar ratios [4–6, 8, 9] and the components are arranged in the lattice structure randomly as shown in Figure 2 for CoCrFeNi and CoCrFeMnNi.
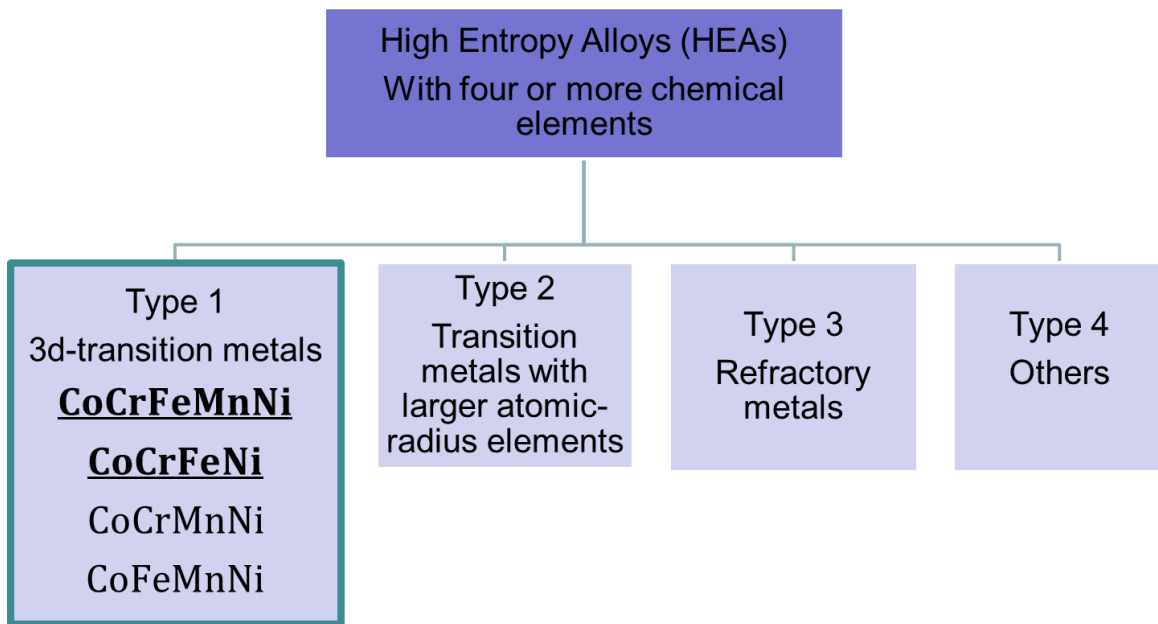
Figure 1: High entropy alloys types. (Recreated from Diao et al. [10])
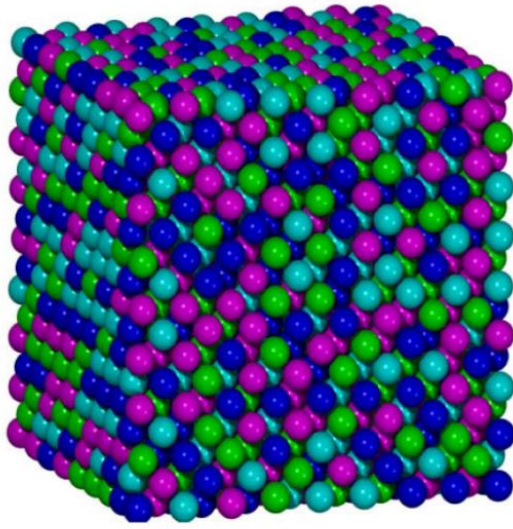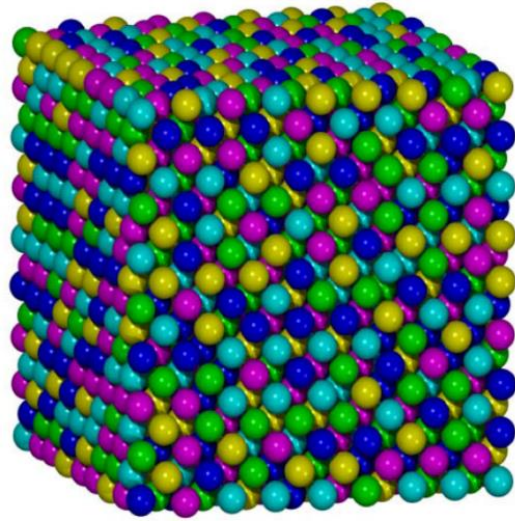
Figure 2: Atoms arrangement in the lattice for (a) FCC FeCoCrNi and (b) FCC CoCrFeMnNi (Source: [11])

Mechanical properties of HEAs such as yield and ultimate strength, ductility, hardness and fracture toughness were found to be in the same range or better than conventional metal alloys like stainless steel and nickel-base superalloy [1–4, 9, 10, 12–14]. Figure 3 shows the toughness versus yield strength Ashby chart of different materials at 77K [10]. High fracture toughness and simultaneous high yield strength of HEAs compared to other materials can be observed from the chart. Figure 4 shows the yield strength of different groups of HEAs at different temperatures compared to five conventional metal alloys which shows that the yield strength of HEAs at a range of temperature from cryogenic to high temperature is better or comparable with other presented metal alloys.
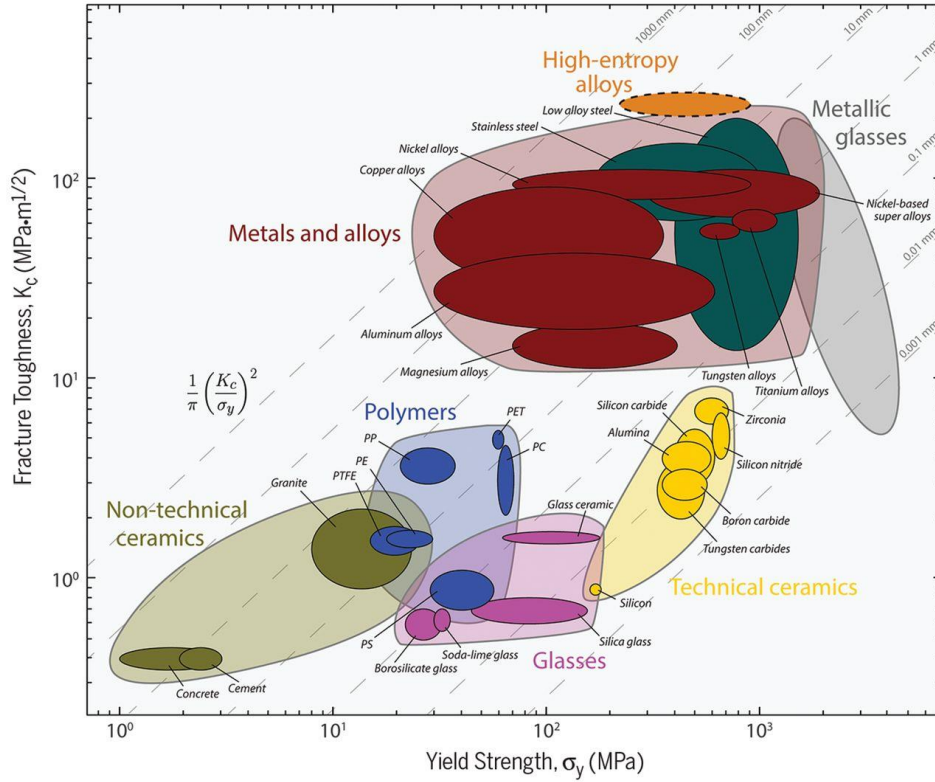
Figure 3: Fracture toughness versus yield strength at 77K Ashby chart (Source: [10])
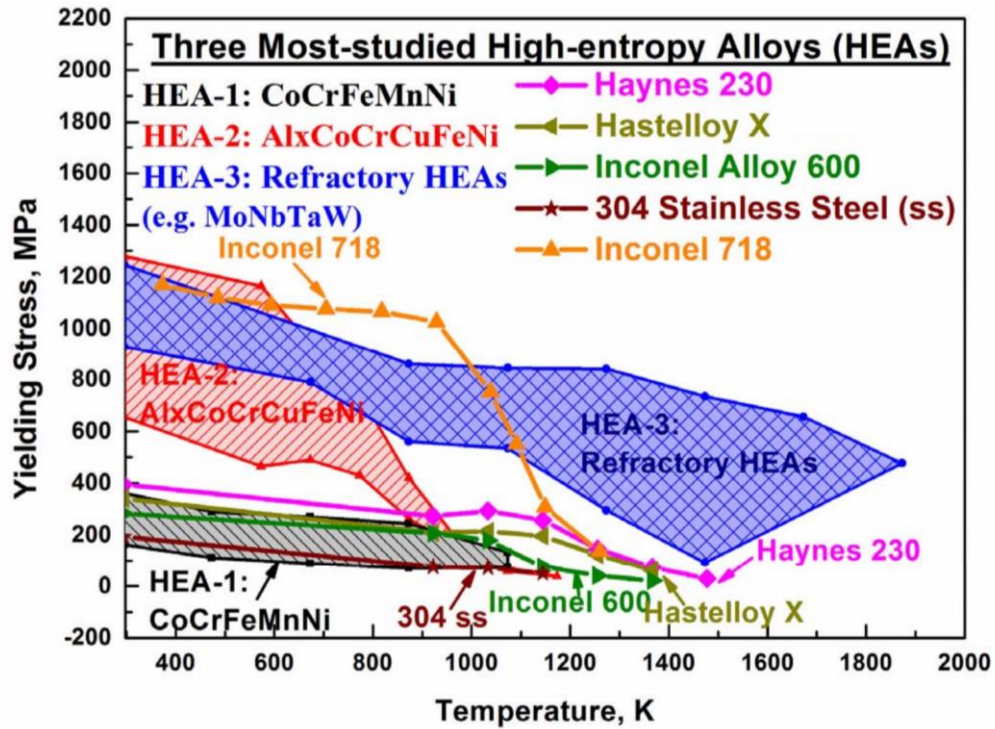
Figure 4: Yield stress of high entropy alloys and conventional metal alloys for a range of temperature from -200K to 2000K (Source: [10])

As mentioned before, It has been proposed that in HEAs the solid phase stabilization is due to the high configurational entropy which has an effect on the Gibb's free energy [4, 5]. Albeit, the phase stabilization effect relation to the high entropy of configuration has been challenged by some recent studies [6, 15, 16].

CoCrFeMnNi High Entropy Alloy

CoCrFeMnNi (Cantor Alloy) [5], is an equi-atomic HEA that has been studied thoroughly under quasi-static tension, quasi-static and dynamic compression, fatigue loading etc. [1, 2, 5, 9, 13, 17–21]. Cantor alloy is a single-phase alloy with face-centered cubic (FCC) structure from the HEA subgroup of type 1 or 3d-transition metals. The fact that CoCrFeMnNi in 20% proportions, has one crystal structure which is FCC is interesting and wouldn't have been predicted before it being developed for the first time by Cantor et al. [5]. Among the five components of the Cantor alloy only Nickel has FCC structure. Cobalt has a hexagon close-packed structure, iron and chromium have body-centered cubic structures and manganese has alpha manganese structure which makes it more unpredictable for the cantor alloy to have only FCC lattice structure.

Under tensile loading the deformation of this alloy is mainly by deformation slip [13, 19]. At high strains of more than 20%, and commonly at cryogenic temperatures, deformation twinning was observed in addition to dislocation slip [9, 20, 21]. Similar behavior of higher strength and ductility due to the activation of twins can be seen in twinning induced plasticity (TWIP) steels [22–26].

Microstructure and mechanical behavior of Cantor alloy in room temperature to 800 °C was studied in the work of Licavoli et al. They described the Cantor alloy manufacturing process to be

able to get to a single phase homogenous structure. They found out that the mechanical properties of Cantor alloy is better than or comparable to 300-series austenitic stainless steel [1].

Otto et al. studied the tensile behavior of Cantor alloy at different temperatures and with different microstructures i.e. different grain sizes. For all of the three grain sizes they studied, they found that with decreasing the temperature, yield and ultimate strength increase. They also observed an increase in the ductility with decrease of the temperature. They attributed the improvement of yield and ultimate strength and the ductility to the activation of nano-twins at cryogenic temperature [13].

Gludovatz et al. studied the fracture resistance of Cantor alloy at cryogenic temperature. They observed an improvement in the mechanical properties with decreasing the temperature. They attributed this improvement to the activation of deformation nano-twinnings [9].

Wang et al. studied the mechanical properties and microstructure of Cantor alloy under high strain rate compression. They observed that as the strain-rate increased, the dynamic yield strength also increased. They also modeled the dynamic flow behavior using the Zerilli-Armstrong plastic model [27].

CoCrFeNi High Entropy Alloy

From the same subgroup, the CoCrFeNi HEA also is a single phase alloy with FCC crystal structure. While there have been studies on its mechanical behavior and microstructure [5, 8, 13, 14, 17], less research has been focused on the CoCrFeNi HEA. Huo et al. studied the tensile quasi-static strain-rate effect of CoCrFeNi and found an increase in the yield and ultimate strength and ductility with rising strain-rate [8]. Gali et al. studied the quasi-static tensile behavior and

microstructural changes of CoCrFeNi at temperatures ranging from -196°C to 1000°C. They found that the strength decreased with increasing temperature, but the strain-rate dependence was relatively weak [14]. Also, as the temperature decreased the ductility increased. They attributed this change to the formation of nano-twins, similar to the findings for CoCrFeMnNi HEA [9].

Huo et al. studied the strain rate effect on CoCrFeNi's quasi-static tensile behavior and observed a shift in the dominant deformation mechanism from dislocation motion at the lower strain-rate of 1×10^{-3} s^{-1} to stacking faults at higher strain-rate of 1×10^{-2} s^{-1} [8].

1.1.2 Digital Image Correlation

Digital image correlation (DIC) is an optical technique which can be used in experimental mechanics field to capture the full-field deformation without having contact with the sample. In this technique the sample field of interest is covered by a random speckled pattern using paint, powder etc. The speckled pattern should have certain characteristics for the digital image registration (i.e. matching) to be possible [28]. For instance, the size of the speckles, the contrast of the pattern, randomness of the black and white colors in the pattern etc. are important in reducing the noise and maknig the image matching possible. During the mechanical test, one or more cameras with suitable lenses are set up such that images can be acquired from the sample field of interest. Enough lighting should also be provided at the field of interest. Depending on the purpose of the test, the frame rate and capture rate of the camera should be set. Camera set-up for using DIC for a tensile experiment can be seen in Figure 5.

Once the images are captured, using an already available software like VIC-2D from Correlated Solutions or by using a code written for this purpose the full field deformation and the strain of

the field of interest can be found. The first captured picture will be considered as the reference,

then movement of the subsets of speckles will be tracked at each proceeding pictures to then be

compared with the reference [28]. Figure 6 is showing the strain field on a sample under tension

which was found using DIC. DIC technique as a full-field deformation measuring technique is

becoming more popular among experimental mechanics community [18, 29–31].

Figure 5: Camera set-up to use DIC for the tensile experiment
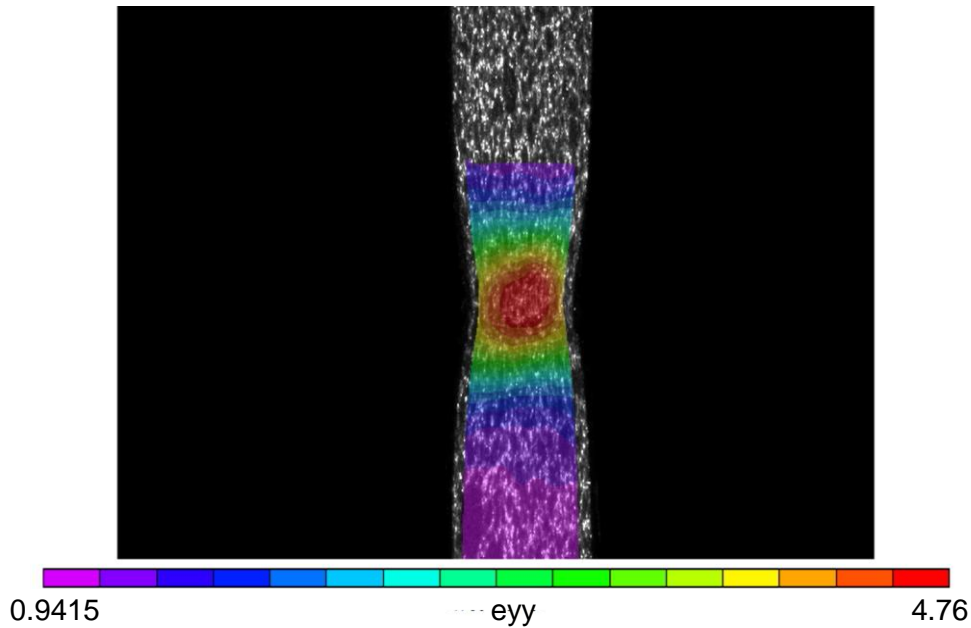
Figure 6: Strain field for a steel sample under tension found using digital image correlation (DIC)

1.1.3 Plastic Deformation Mechanisms

After a material reaches its yield point, it undergoes plastic deformation. There are different modes of plastic deformation that can happen depending on the material, its structure and the external loading condition. Planar slip and twinning are two main modes of metal plastic deformation.

Planar slip is one of the main modes of plastic deformation in metals. In planar slip, blocks of crystal slide on one another on desirable crystallographic planes called slip planes and in directions called slip direction. Slip plane is the plane with more atomic density and the slip direction is the closed pack direction of the slip plan. In the FCC structure, the {1 1 1} planes and the <1 1 0> directions are the slip systems [32]. During the slip, crystal orientations remain the same and the crystal atoms slide the same amount which can be seen in Figure 7. Slip is commonly seen in body centered cubic and face centered cubic crystal structures.

Stress needed for slip in perfect crystals is very high but, crystals are not perfect. Crystals contain dislocations that can move. If the dislocations lie at the position of symmetry of the atoms in slip plane, the lattice do not show any resistance to the motion of them and therefore a small force can be enough for their movement. This small force is called the Peierls-Nabarro force. Movement of dislocations can result in surface step or slip band [32, 33]. Therefore, the force that is needed for dislocation planar slip is small. For slip to occur the critical resolved shear stress for slip should be achieved.
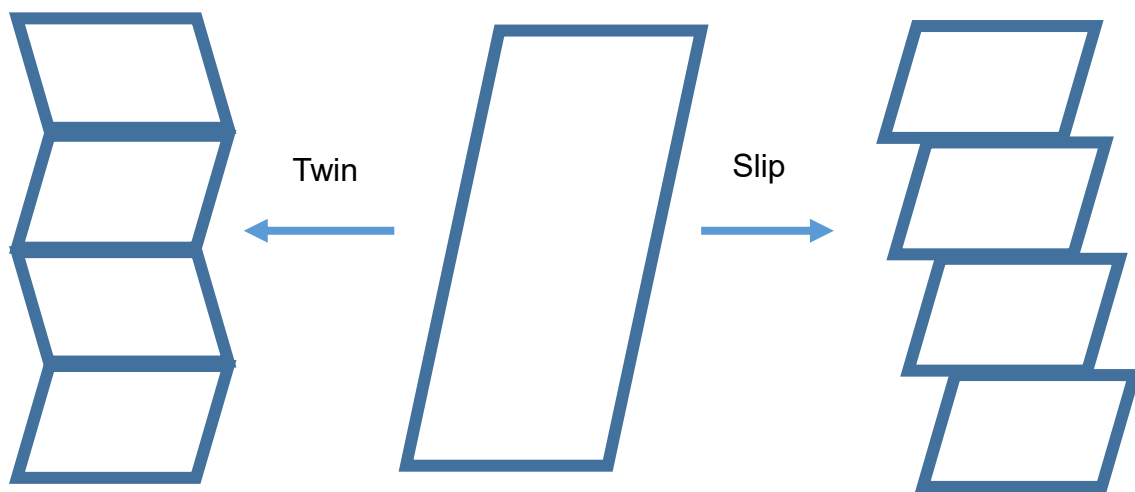
Figure 7: Schematic showing the difference between slip and twinning deformation modes

Another important plastic deformation mechanism in metals is twinning. Twinning occurs when part of the crystal changes its orientation in symmetry with the untwinned part of the crystal. The twin part is the mirror image of the crystal before twinning also known as the parent crystal. The symmetry plane between the twinned and untwinned parts is called the twinning plane. Figure 8 shows an atomic picture of twinning.
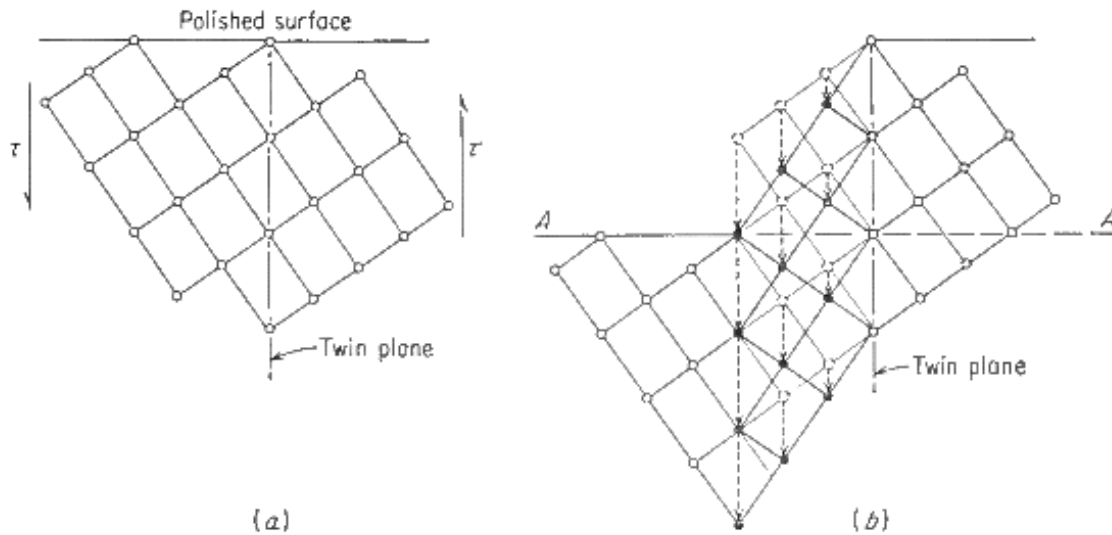
Figure 8: Classical picture of twinning (Source: [32])

Twinning can be explained as the intergrowth of two crystals in a symmetric way [34]. After twinning the crystal lattice axis changes and the twinned lattices are mirrored with respect to the twinning plane. The difference between slip and twin has been shown schematically in Figure 7. Twinning can happen during the manufacturing process. These twins are called annealing twins. Also, there are twins that occur as a mode of plastic deformation called deformation twins. Deformation twins are commonly observed in hexagonal close pack structures and metals with low stacking fault energy. The stress needed for the twin nucleation is called the critical resolved shear stress for twinning.

1.1.4 Adiabatic Shear Bands

In high strain-rate loading the shear strain localizes in narrow regions called shear bands. Adiabatic shear bands which are regions with intense deformation due to shear localization, occur when a material deforms adiabatically. Based on the Zener and Hollomon theory, Due to the strain hardening the stress increases and at the same time it is lowered due to thermal softening [35]. Therefore it can be said that strain hardening and stain rate hardening are

opposing factors and geometric and thermal softening are the favoring factors for the formation of adiabatic shear bands [36].

1.2 Motivation

Portions of this section are included in papers submitted for review.

High-entropy alloys (HEAs) provide a viable replacement to conventional materials (e.g. stainless steel and nickel-base superalloy) in critical load-bearing applications because of their high strength, ductility, fracture resistance and corrosion resistance, some even down to cryogenic temperatures [6, 8, 9, 13, 14, 21, 37]. Structural materials need to have both high strength and high ductility, but these two properties are usually inversely proportional to each other in conventional metal alloys. This trade-off has caused challenges in the development of high performance metal alloys [8]. Conventionally, metal alloys are developed by selecting the main component based on the most important property required. Then, alloying elements are added to provide other needed properties [4, 5, 9].

It is necessary to study the behavior of materials under different strain-rates. Depending on the material, the strength, ductility and work hardening rate may increase or decrease with the increase in strain-rate [3, 8, 27]. As mentioned before there have been studies on the tensile behavior of both CoCrFeNi and CoCrFeMnNi in the quasi-static strain-rate range and dynamic strain rate experiments in compression. No work has been done on the tensile behavior and microstructure of both CoCrFeNi and CoCrFeMnNi in the range of strain rates from quasi-static to dynamic.

The effect of strain-rate on the mechanical properties and microstructure of CoCrFeNi and CoCrFeMnNi needs further study. Also, the underlying deformation mechanisms responsible for these effects are of interest to support future alloy development and inform physics-based models. To understand the effect of strain-rate on the mechanical behavior and microstructure of CoCrFeNi and CoCrFeMnNi HEAs, tensile experiments were performed at strain-rates from 10^{-4} to 10^3 s^{-1}. The microstructures of the HEAs were studied using electron backscatter diffraction (EBSD) before deformation and transmission electron microscopy (TEM) post-mortem.

Chapters Overview

Chapter 2 introduces the materials and methods used to prepare the samples, run the experiments and use electron microscopes for microstructural characterization. Chapter 3 presents the results and discuss the results from the mechanical testing and electron microscopies. Chapter 4 includes the main conclusions and discusses the proposed future work of this research. Chapter 5 lists the references used in this research.

Chapter 2. Materials and Methods

Portions of this section has been submitted as part of a journal paper for review to a journal.

2.1 Processing and Chemical Composition

The HEAs in this study, CoCrFeNi and CoCrFeMnNi, were produced by induction melting and computationally-based homogenization heat treatments. The alloys were machined to clean up the surfaces, preheated to 975°C and hot worked by forging and rolling to a nominal thickness of 0.16 mm. Following the last roll pass the plates were reheated for five minutes and air cooled. CoCrFeNi and CoCrFeMnNi HEAs will be referred to as HEA-1 and HEA-2 respectively throughout the rest of this paper. Table 1 shows the chemical composition of HEA-1 and HEA-2.

	Mn	Cr	Ni	Co	Fe	C	N	O	S
	wt.%	wt.%	wt.%	wt.%	wt.%	ppm	ppm	ppm	ppm
HEA-1	0.026	22.86	26.41	25.47	25.11	260	60	60	20
HEA-2 (Cantor)	19.60	19.37	21.32	21.47	18.15	274	84	4	13

Table 1: Chemical compositions of HEA-1 and HEA-2.

The mixing enthalpy, atomic size difference and mixing entropy of both HEA-1 and HEA-2 were calculated using their chemical composition to show that they fall within the acceptable range of being considered a high entropy alloy.

For HEA-1 ΔH_{mix}= -3.64 $kJmol^{-1}$, δ=1.06% and ΔS_{mix}= 11.51 $JK^{-1}mol^{-1}$ and for HEA-2, ΔH_{mix}= -4.3 $kJmol^{-1}$, δ= 0.92% and ΔS_{mix}= 13.36 $JK^{-1}mol^{-1}$. The values are within the range to form a solid solution [2, 25, 26].

2.2 Mechanical Testing

Flat dog-bone shaped specimens with a gauge length of 16 mm, width of 3 mm and thickness of 2 mm were made from the HEA-1 and HEA-2 plates using electro-discharge machining. Figure 9 shows and schematic of the geometry of the dog-bone specimens.

Figure 9: Schematic of the dog-bone specimen geometry in inches
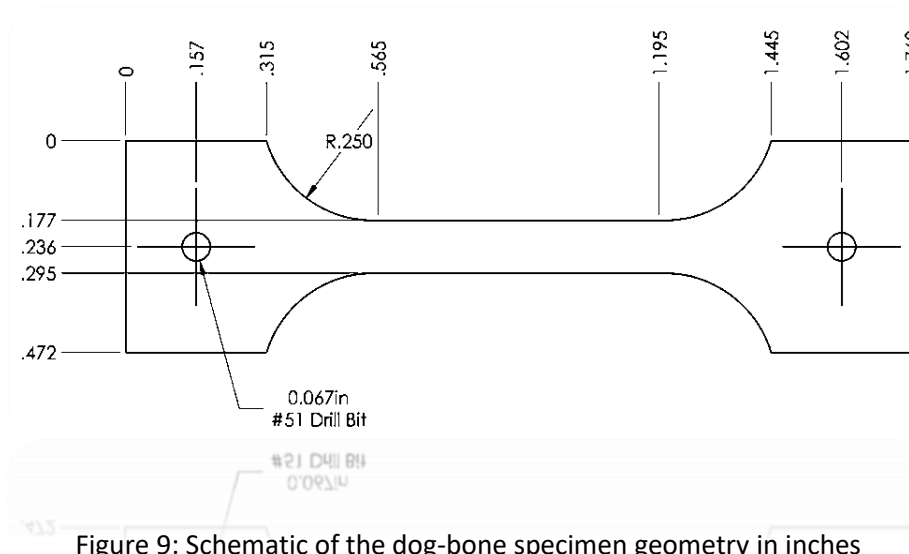
All uniaxial tensile experiments were performed at room temperature. The quasi-static experiments were performed at strain-rates of 2×10^{-4}, 1.5×10^{-3}, 1×10^{-2}, 1×10^{-1} and 3×10^{-1} s^{-1} using an MTS Landmark 370 servo hydraulic load frame. Strains were measured using digital image correlation (DIC) for strain-rates of 2×10^{-4}, 1.5×10^{-3}, 1×10^{-2} s^{-1} using a Point Grey GS3 camera with 0.5x Navitar lens. One side of the specimens were grinded and polished using Buehler EcoMet™ 3 grinder-polisher up to P4000 and speckled using black paint. For the 1×10^{-1} and 3×10^{-1} s^{-1} strain-rates, strains were measured using an MTS extensometer with a 12 mm gauge length. These two tests were performed by our collaborator Joe Indeck and Dr. Hazeli from University of Alabama in Huntsville. Figure 10 shows a set-up of

the specimen in MTS load frame. DIC analyses were performed using VIC-2D from Correlated Solutions.
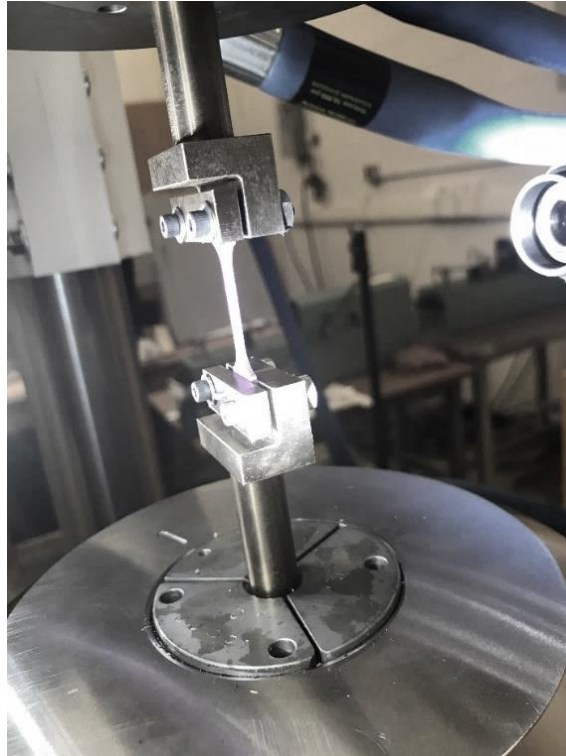
Figure 10: Specimen set up in MTS load frame

Dynamic experiments, strain-rates of 183, 389, 495 and 980 s^{-1} for HEA-1 and 403, 409, 635 and 1000 s^{-1} for HEA-2, were performed using a modified Split-Hopkinson Pressure Bar (SHPB). The dynamic specimens had a gauge section 6 mm wide and 1.5 mm thick. Strain in the specimen was measured with DIC. A Shimadzu HPV-2 high speed camera with a Tamron 180mm macro lens was used to record deformation of the specimen at either 250,000 frames per second (fps) or 500,000 fps depending on the striker bar length. All the dynamic tests were done by our collaborator Joe Indeck and Dr. Hazeli from University of Alabama in Huntsville. DIC analyses were performed using VIC-2D from Correlated Solutions.

Figure 11: Split Hopkinson pressure bar (Provided by Joe Indeck from Dr. Hazeli's research group (MMEE) University of Alabama in Huntsville.)

2.3 Microstructure Characterization

Electron backscattered diffraction (EBSD) was performed on HEA-1 and HEA-2 samples before testing using a Hitachi SU6600 scanning electron microscope (SEM) at 20 kV. The specimens were polished based on the Beuhler Guide on materials preparation (For NiCrFe Alloys) and then vibro-polished before EBSD. Figure 12 shows the diamond pastes, polisher and the vibor-polisher used to prepare the samples for EBSD. The vibro-polishing was done for 30 hours.

Analysis with transmission electron microscopy (TEM) was performed on the post-mortem specimens. Foils of thickness 80-90 nm were prepared with a focused ion beam technique using a Hitachi NB5000 from an area close to the fractured surface of the specimens (Figure 13). TEM

was performed using a Hitachi H-9500 high resolution transmission electron microscope at 300

kV.

Figure 12: Diamond pastes, polisher and vibro-polisher used to prepare the samples for EBSD.
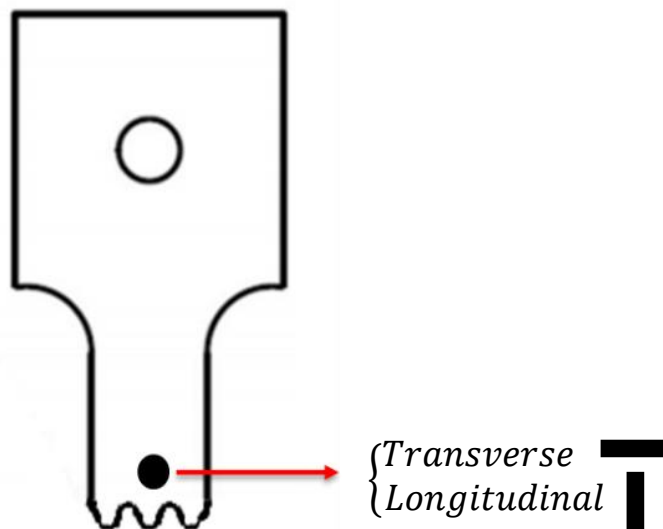
Figure 13: Schematic of the position of the TEM samples on the fractured specimen.

2.4 Initial Microstructures

The EBSD maps of the grain orientations of HEA-1 and HEA-2 are shown in Figure 14. Using ellipse

fitting method in AZtecHKL software, the average grain size was found. The average grain size

was 21.84 μm for HEA-1 and 23.87 μm for HEA-2. The average grain sizes of HEA-1 and HEA-2 are

similar; therefore, the Hall-Petch effect can be disregarded. Annealing twins were observed in

the microstructure of both HEAs which is common in FCC materials [17].
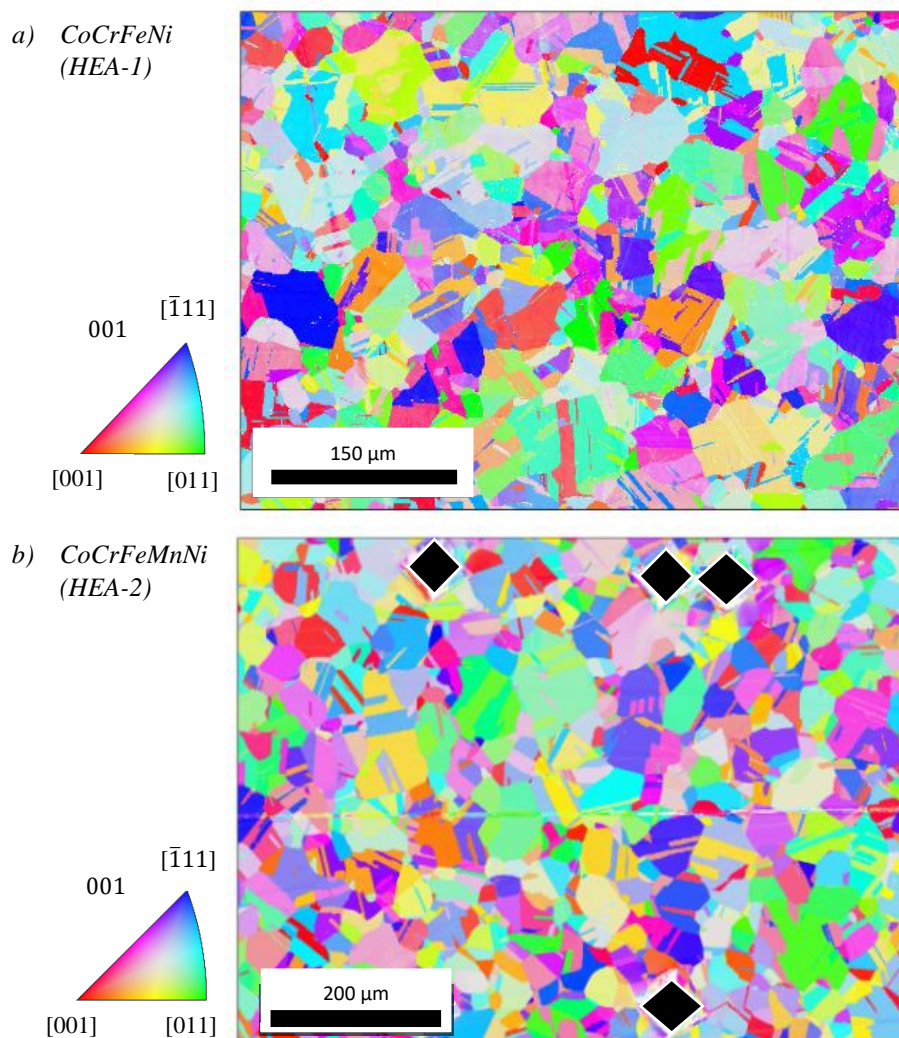
Figure 14: EBSD IPF Z map using SEM denoting the grain orientation of a) HEA-1 with the average grain size of 21.84 μm and b) HEA-2 with the average grain size of 23.87 μm. Annealing twins are present in both HEA-1 and HEA-2 orientation maps. The black squares are the Vickers micro-indentations to identify the area of interest.

Chapter 3. Results and Discussion

This section has been submitted as part of a journal paper for review to a journal.

3.1 Tensile Mechanical Properties

Engineering stress versus engineering strain curves obtained from HEA-1 and HEA-2 tension experiments for quasi-static strain-rates are summarized in Figure 15 and Figure 16, respectively. There was an increase in yield strength for higher strain-rates.
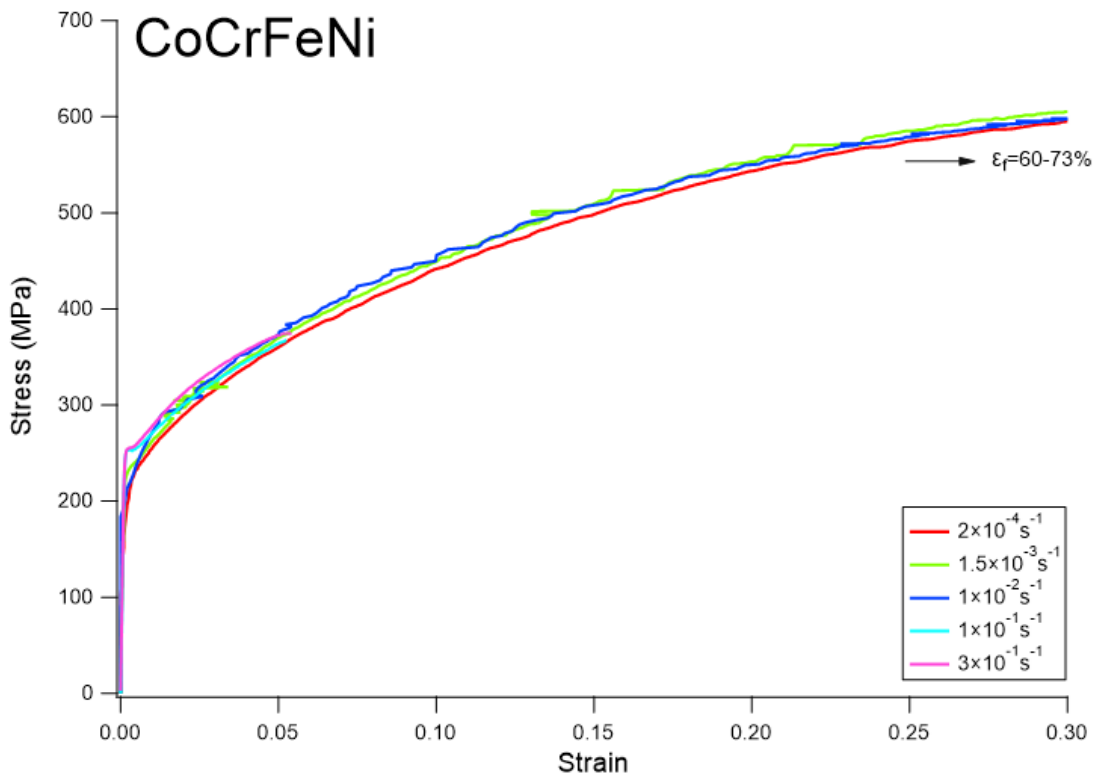
Figure 15: Engineering stress-engineering strain curves of HEA-1 under uniaxial tensile test with different strain- rates.
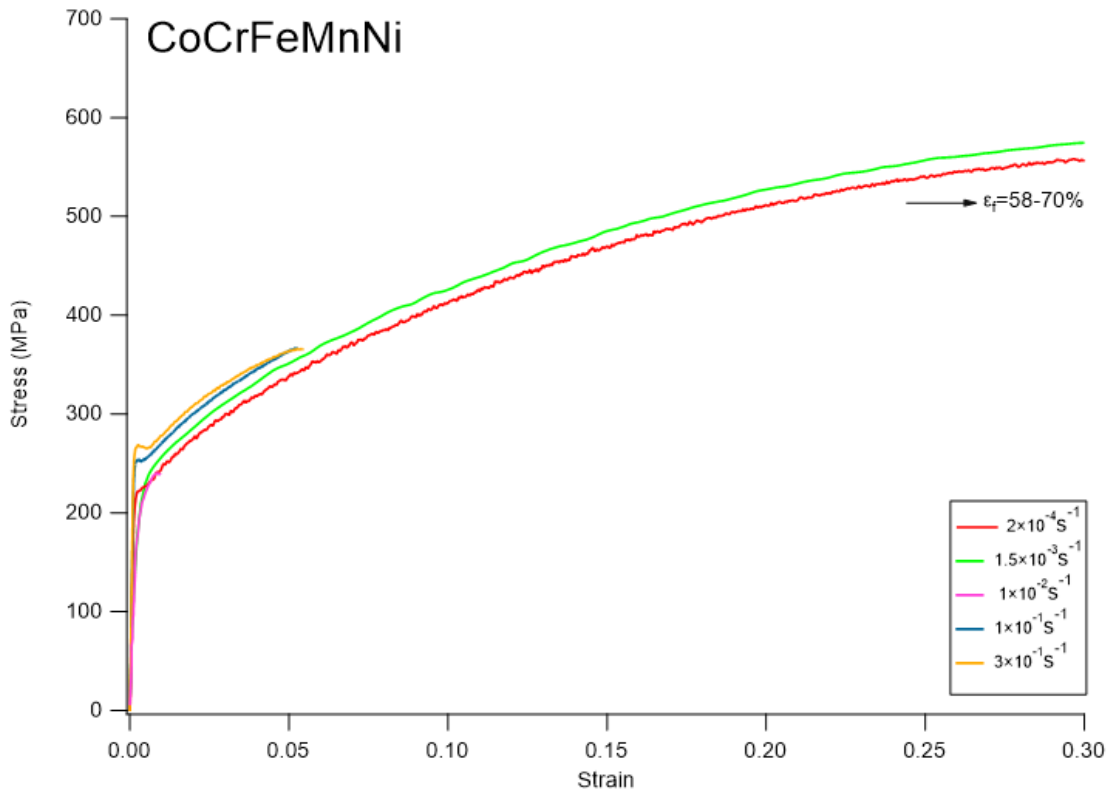
Figure 16: Engineering stress-engineering strain curves of HEA-2 under uniaxial tensile test with different strain- rates.

The mechanical properties of HEA-1 and HEA-2 from the quasi-static tensile experiments are listed in Table 2 and Table 3 respectively. Yield strength and ultimate strength were larger in magnitude for HEA-1 in comparison to HEA-2 in the quasi-static strain-rate range. The yield strength and ultimate strength magnitudes were within the range that has been reported in Diao's et al. review paper [10]. The area reduction magnitudes were similar for both HEA-1 and HEA-2. Samples subjected to 1×10^{-1} and 3×10^{-1} s^{-1} strain-rates did not reach their ultimate strengths due to experimental limitations, and therefore, ultimate strength and area reduction percentage data was not reported. Low yield stress and high work hardening was observed from the stress-strain curves of both HEA-1 and HEA-2. This is similar to the tensile behavior of

austenitic stainless steel [25]. The mechanical properties were similar for all quasi-static strain-rates, suggesting that changes in strain-rates did not affect the tensile properties in the quasi-static range.

	HEA-1				HEA-1 at RT (source: [10])
Strain Rate (s^{-1})	2×10^{-4}	1.5×10^{-3}	1×10^{-2}	1×10^{-1}	
Yield Strength (MPa)	230	232	240	257	290-300
Ultimate strength (MPa)	625	613	608		620-700
Area Reduction %	63	73	73		

Table 2: Mechanical properties of HEA-1 under uniaxial tensile test with quasi-static strain rates.

	HEA-2				HEA-2 at RT (source: [10])
Strain Rate (s^{-1})	2×10^{-4}	1.5×10^{-3}	1×10^{-2}	1×10^{-1}	
Yield Strength (MPa)	215	228	240	253	210-250
Ultimate strength (MPa)	553	594	560		550-600
Area Reduction %	67	70	70		

Table 3: Mechanical properties of HEA-2 under uniaxial tensile test with quasi-static strain rates.

Strain-rate sensitivity (SRS) values were calculated to further investigate the effect of strain-rate on the mechanical properties of HEA-1 and HEA-2. The SRS value m can be defined by:

$$m = \frac{dln\sigma}{dln\dot{\varepsilon}}$$ (1)

where σ and $\dot{\varepsilon}$ represent the flow stress and strain-rate, respectively [40]. The SRS value usually varies between zero and unity for metals [36]. Figure 17 shows the log-log and semi log plot of flow stress at strain of 0.03 and strain rate respectively. The flow stress SRS was found to be

m=0.044 for HEA-1 and m =0.048 for HEA-2. Positive m values suggested that the mechanical properties of HEA-1 and HEA-2 improved with the increase of strain-rate, which is desirable. The flow stress SRS was low in the beginning of the quasi-static range. The SRS value was greater for HEA-2 in the entire range of strain-rates studied, indicating that the flow stress of HEA-2 was more sensitive to changes in strain-rate. The high strain-rate sensitivity at dynamic strain-rates was believed to be related to the distorted lattice of the HEAs [41] and/or thermally activated mechanisms [42]. Moon et al. found the SRS component of 0.026 by running strain-rate jump experiments on Cantor Alloys with average grain size of 13 μm. The sensitivity variable β, found from the semi-log relation was found to be 32 MPa for HEA-1 and 35 MPa for HEA-2.
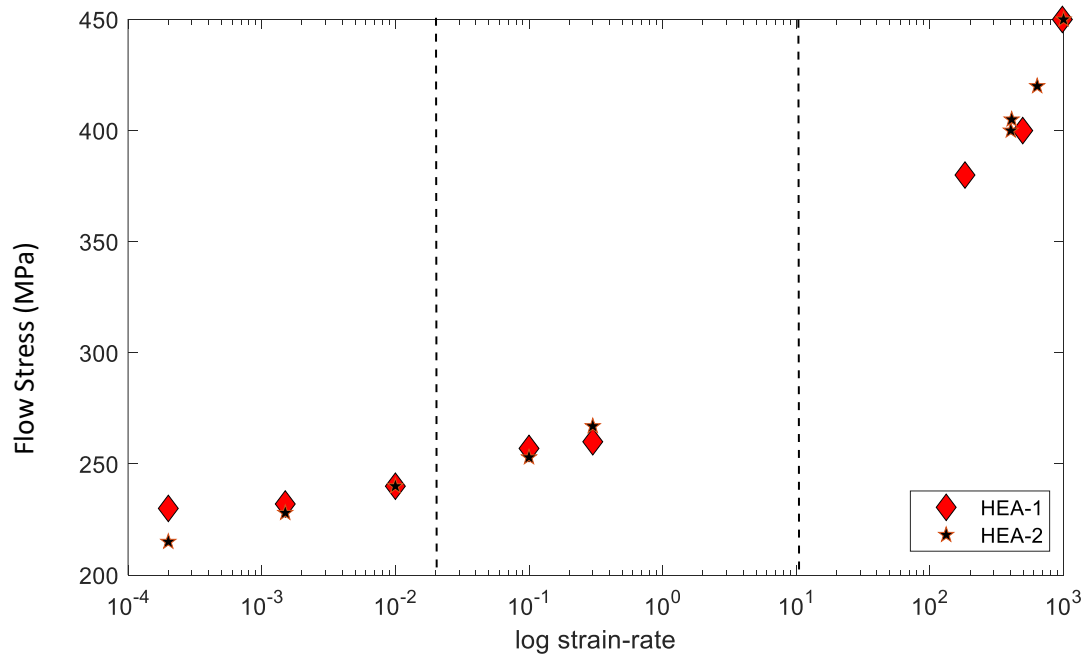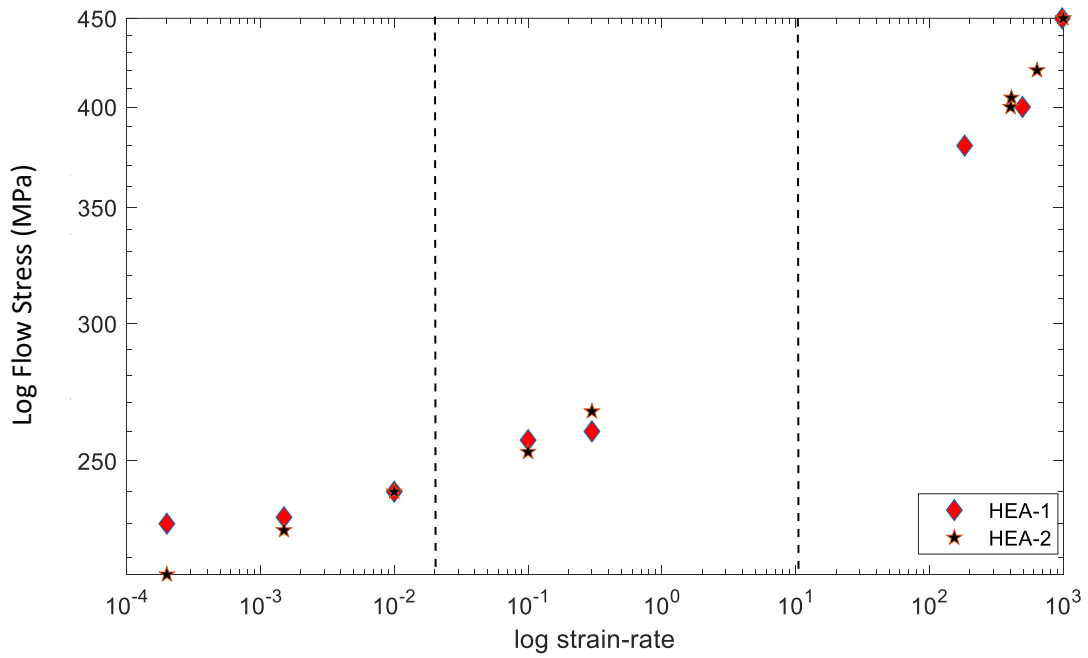
Figure 17: Flow stress at strain of 0.03 versus strain-rate in logarithmic and semi-logarithmic forms for HEA-1 and HEA-2 at three different strain-rate zones showing the increase in SRS of both HEAs with the increase of strain-rate.

Strain-hardening rates (SHRs) shown in Table 4 and Table 5, were found for HEA-1 and HEA-2 from the true stress and true strain values. True stress-true strain curves are shown in Figure 18 for all strain rates ranging from quasi-static to dynamic. The portion of the graphs used to find the SHR values is shown.
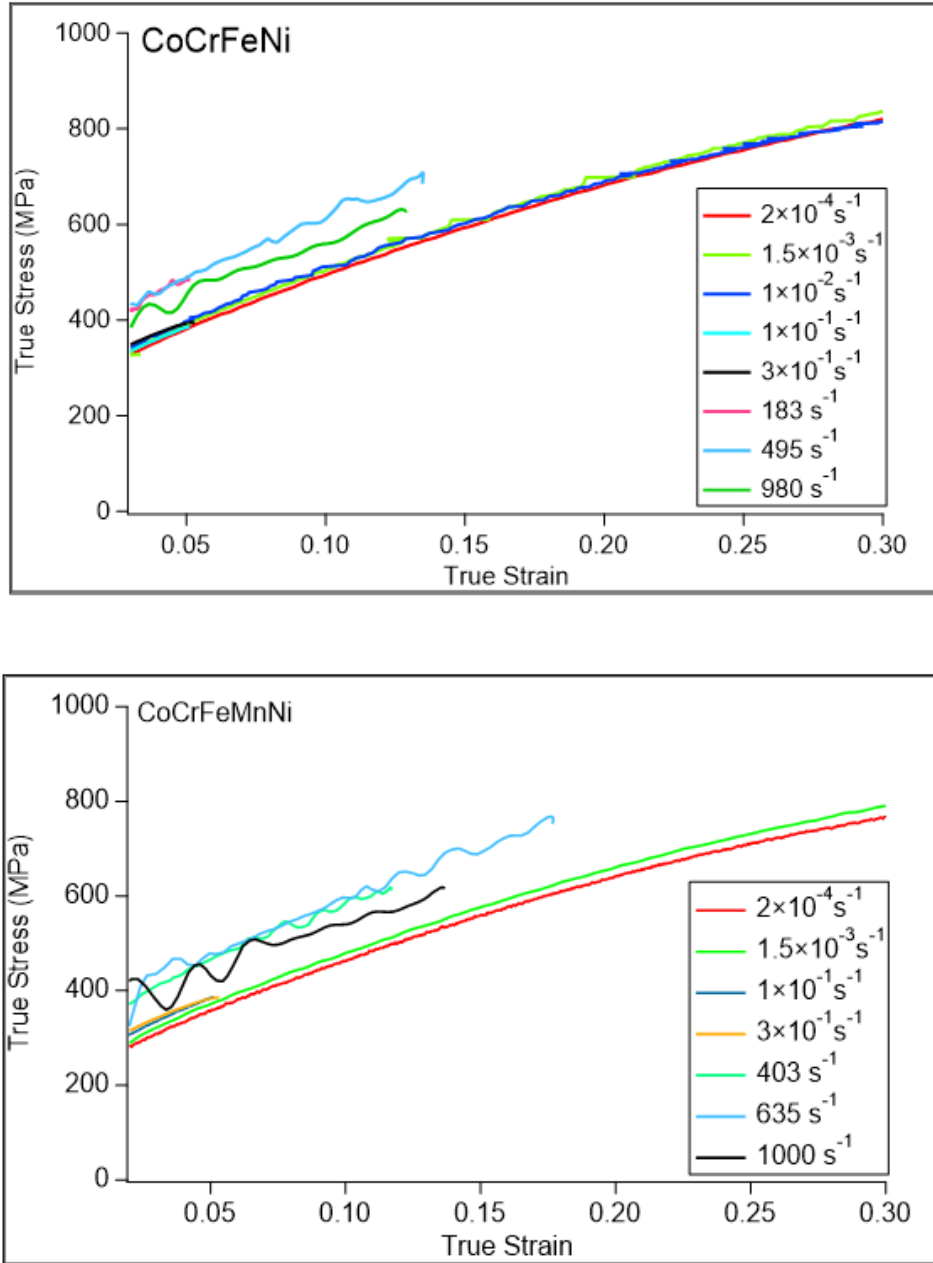
Figure 18: HEA-1 and HEA-2 true stress-true strain curves for all strain rates ranging from quasi-static to dynamic. The portion of the graphs used to find the SHR values is shown.

The SHRs of HEA-1 were greater than that of HEA-2 except at 2×10^{-4} s^{-1}. The SHRs were higher for the dynamic strain-rates for both HEAs. HEA-1 SHRs showed a fluctuating value in the quasi-static range, initially increasing 28% then subsequently decreasing 12% for the strain rate of to 1×10^{-2} s^{-1}. In the dynamic range, SHR for HEA-1 increased between 183 s^{-1} to 389 s^{-1} and then decreased when the strain-rate was further increased to 495 s^{-1} and 980 s^{-1}. HEA-2 SHR decreased with the increase of strain-rate throughout the quasi-static range from 2×10^{-4} s^{-1} to 1×10^{-2} s^{-1}. In the dynamic range, the SHR for HEA-2 was greatest at a strain rate of 403 s^{-1}. As the strain-rate increased from 403 s^{-1} to 1000 s^{-1}, the SHR continued to reduce similar to the quasi-static behavior. For both HEA-1 and HEA-2 variation of the SHRs within the quasi-static range and dynamic range is negligible. Their higher SHRs at dynamic strain-rates were because of the activation of nano-twins and the effects of the Dynamic Hall-Petch effect [18, 20]. A similar response has been identified in TWIP steels, including the extensive ductility [22]. The higher SHRs due to the nano-twins activation resulted in necking to be delayed and the ductility to be increased [1, 6]. The SHRs decreased at the highest strain-rates in the dynamic range due to the adiabatic nature of the dynamic experiments which caused an increase in temperature. This temperature rise caused material softening that repressed the formation and growth of nano-twins [35].

HEA-1	**Quasi-Static**			**Dynamic**			
Strain Rate (s^{-1})	2×10^{-4}	1.5×10^{-3}	1×10^{-2}	183	389	495	980
Strain hardening rate (GPa)	1.59	2.04	1.80	2.79	2.87	2.33	2.1

Table 4: HEA-1 strain hardening rates at quasi-static and dynamic strain-rates.

HEA-2	Quasi-Static			Dynamic			
Strain Rate (s^{-1})	2×10^{-4}	1.5×10^{-3}	1×10^{-2}	403	409	635	1000
Strain hardening rate (GPa)	1.75	1.68	1.58	2.31	2.26	2.25	1.94

Table 5: HEA-2 strain hardening rates at quasi-static and dynamic strain-rates.

Twinning formation and growth happened because of the low stacking fault energies (SFEs) of these HEAs. The SFEs of HEA-1 and HEA-2 have been calculated to be approximately 30-33 mJm^{-2} [29, 30] and 20-25 mJm^{-2} [21], respectively, which are within the preferential range for twinning formation [22].

3.2 Microstructural Changes Resulting from Tensile Deformation

TEM micrographs were captured on foils prepared from an area close to the fracture surface of the deformed samples to further investigate the deformation mechanisms activated during the tensile experiments. The deformation twin nucleation critical resolved shear stress (CRSS) for the Cantor alloy has been identified [8, 15, 16]. Abuzaid et al. found the CRSS for slip and twin nucleation in the Cantor alloy with single crystals at room temperature and 77K [19]. In a further refinement, Laplanche et al. found the tensile stress at which twinning occurs to be roughly independent of temperature and occur at 720±30 MPa for polycrystalline Cantor alloy, from which they deduced a CRSS for twinning of 235±10 MPa [21]. Although the global tensile stress on the sample reached a magnitude that presumably would satisfy the CRSS for twinning being reached, no twinning was observed in the post-mortem TEM micrographs of HEA-2 specimens under quasi-static strain-rates. This may be due to the small area investigated, as previously

discussed in [21]. No twinning was observed in the HEA-1 TEM micrographs of the specimens loaded at quasi-static strain-rates either. As shown in the Figure 18 TEM micrographs of HEA-1 and HEA-2, post-mortem samples under dynamic strain-rates both contained nano-twins of widths 26 - 29 nm and 7 - 24 nm for HEA-1 and HEA-2 respectively. Selected nano-twins and their widths are identified in the micrographs. The lack of nano-twins in the quasi-static samples and their presence in the dynamic samples confirmed a transition between dominant deformation mechanisms. In both HEA-1 and HEA-2, the deformation mechanisms shifted from the planar dislocation slip at lower strains, the quasi-static experiments, to deformation by nano-twinning at higher strains, during the dynamic experiments, due to the increased hardening of the material, thus exceeding the critical twinning resolved shear stress.
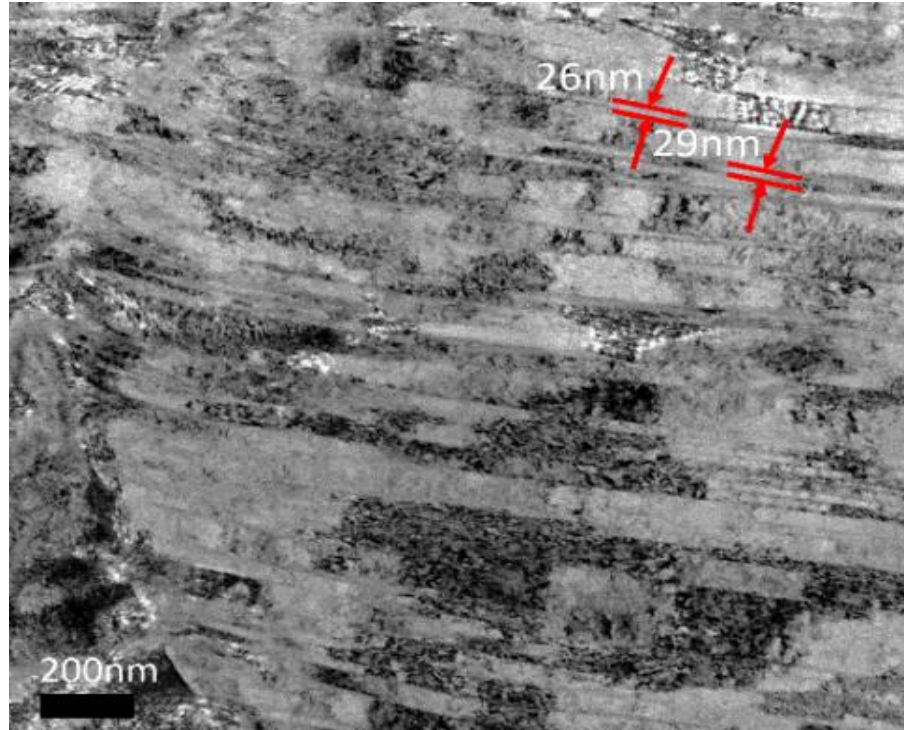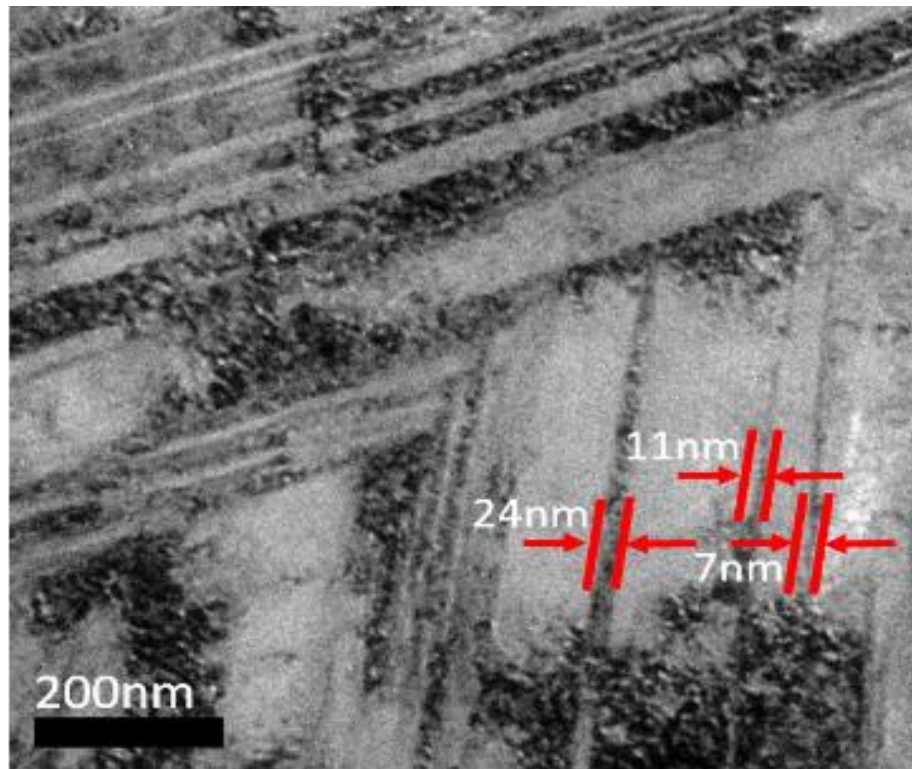
Figure 19: Transmission electron microscope (TEM) micrographs of foils extracted from post-mortem samples subjected to tension at strain rates of 980 s^{-1} and 1000 s^{-1} for (a) HEA-1 and (b) HEA-2. The micrographs were observed near the specimens' fractured surface.

3.3 Effect of the Number of Elements

In a study by Gali et al., the negligible effect of the number of elements (four in the CoCrFeNi to five in CoCrFeMnNi) on the strengthening of the HEAs was observed [14]. It was observed that the HEA-1, with the less configurational entropy, had higher mechanical properties at different strain-rates. The same trend was observed in the work by Laplanche et al. [37]. They studied the mechanical properties of CoCrNi with a lower entropy of configuration compared to CoCrFeMnNi. Both CoCrNi and CoCrFeMnNi had the same initial plastic deformation mechanism of glide at lower strains with the addition of deformation twinning at higher strains. CoCrNi and CoCrFeMnNi both had similar CRSS for twinning, but this stress was reached at lower strain for CoCrNi. This is because of the higher yield strength and work hardening rate of the CoCrNi. In this study, higher SHRs of HEA-1 compared to HEA-2, similarly indicated that as the number of elements decreased in the HEA, the CRSS for nano-twinning occurred at a lower strain resulting in a delay in necking and therefore better strength and ductility of the HEA.

3.4 Compression and Tension Mechanical Properties Comparison

Wang et al. studied the mechanical properties and microstructure of the Cantor alloy under high strain-rate (1×10^3 to 3×10^3 s^{-1}) compression [27]. The dynamic yield strengths ranged from 500-700 MPa, higher than the yield strength range found for dynamic tension. This follows the trend found in the present study where an increase in yield strength coincided with an increase in the strain-rate in the dynamic range. The greater yield strength in Wang's et al. study is attributed to the smaller grain size of their material. Their yield strength SRS value, m, was 0.078 which is lower than the SRS value in our study. The SHRs in the study of Wang et al. were also close to each other with small variations but SHRs increased with the increase of strain-rate

throughout the whole dynamic range. Whereas, in this study an initial increase and then decrease of the SHRs for both HEA-1 and HEA-2 was observed. Serration behavior in the work of Wang et al. was similar to the wave propagation artifacts observed in this study due to the testing technique [36].

Park et al. investigated the compressive strain-rate effect on mechanical properties and microstructure of the Cantor alloy in the strain-rate range of 10^{-4} to 4.7×10^3 s^{-1} [30]. The SRS of the Cantor alloy under quasi-static compression was 0.028, analogous to the tensile SRS in the present study. They also observed an increase in the SRS values from quasi-static to dynamic strain-rates. Their measured yield strengths were 320 and 365 MPa at strain-rates of 10^{-4} and 10^{-2}, respectively. The difference in yield strength for tension and compression can be attributed to the Hall-Petch effect as their average grain size was 16 μm compared to 23.87 μm for HEA-2 in this study. After estimating for the Hall-Petch effect, the yield strengths for HEA-2 in this study were within reasonable agreement of those reported by Park et al.

The tensile and compressive behavior of the Cantor alloy was similar with no differences between deformation mechanisms and similar mechanical properties. Remaining discrepancies can be attributed to differences in the chemical composition and material processing.

Chapter 4. Conclusions and Future Work

This section has been submitted as part of a journal paper for review to a journal.

4.1 Conclusions

The strain-rate effect on the tensile behavior of CoCrFeNi (HEA-1) and CoCrFeMnNi (HEA-2) has been studied through tensile experiments at strain rates ranging from quasi-static,10^{-4} s^{-1}, to dynamic, 10^3 s^{-1}. TEM was performed on post-mortem specimens, and the presence of nano-twins was found in the dynamic samples of both HEAs.

The dominant deformation mechanism of HEA-1 and HEA-2 was observed to shift from dislocation slip at lower strain-rates to deformation by nano-twinning at higher strain-rates. The strain-rate sensitivity component was found to be low for quasi-static strain-rates showing no strain-rate sensitivity and higher for dynamic strain-rates showing positive strain-rate sensitivity for both HEAs. HEA-1 possessed higher yield and ultimate strength for all strain-rates, but HEA-2 showed more strain-rate sensitivity. Both alloys showed promising possible application as structural materials due to their strength, ductility, strain-rate sensitivity and strain hardening rate both in the quasi-static and dynamic strain-rate range.

4.2 Future Work

4.2.1 Nano-Twins Nucleation and Growth Using High Resolution DIC

To further study the mechanical properties of HEA-1 and HEA-2 and relating them to their microstructure, more tensile experiments are necessary. The full-field strain heterogeneity will be found at the area of interest using high resolution DIC using silicon carbide 1200 mesh powder

speckled samples and a microscope with 20x magnification. An EBSD will be done before the

tensile experiments on each sample on the area of interest marked by 5 Vickers micro-indenters.
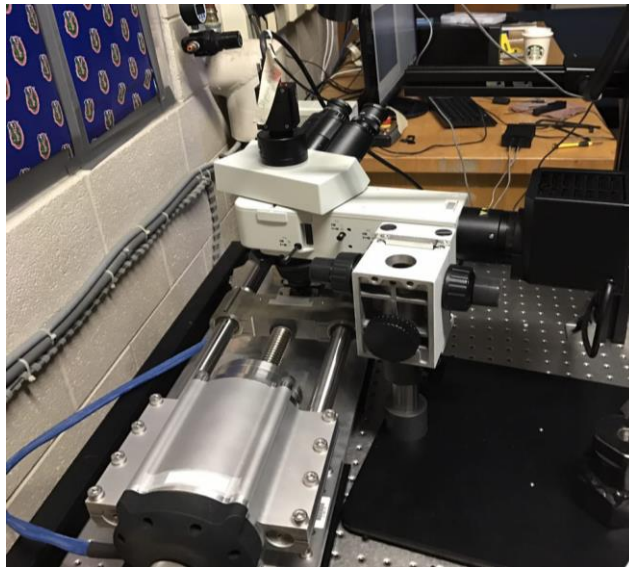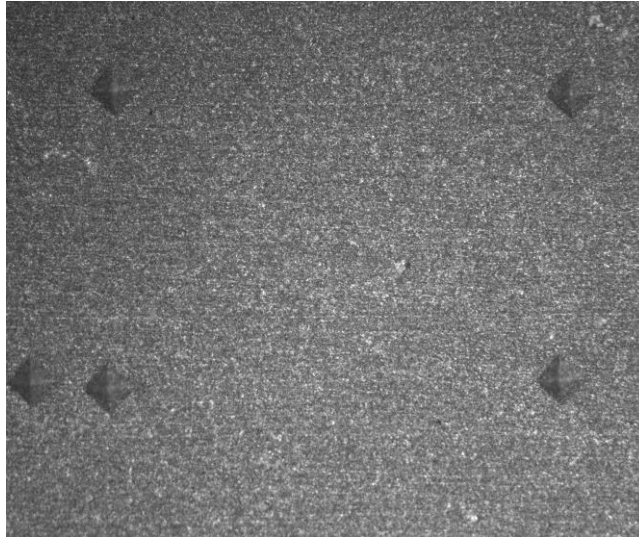

Figure 20: Powder speckled sample with 5 Vickers indentation markers on top and the testing set-up showing the load frame and a DIC set-up with a microscope on the bottom.

The full-field deformation measurements will be aligned with microstructural information from

EBSD to relate local strain and microstructural texture.

Nano-twins - The onset of nano-twins is known to be at high angle grain boundaries. Dog-bone specimens of high entropy alloys CoCrFeNi and CoCrFeMnNi will be grinded and polished using Buehler grinder-polisher down to 0.05 μm abrasive size and then vibropolished using Buehler VibroMet2. Five Vickers micro-indentation marks will be made on the polished surface on the gauge length to specify the area of interest. EBSD will be performed on the samples using a Hitachi SU6600 SEM. The specimens will be powder speckled to have a full-field strain measurement of the specified area using high resolution DIC, with a sub-grain resolution, when tested under tension. After the tensile experiments the full-field deformation measurements will be aligned with microstructure information from EBSD. To study the nucleation and growth of nano-twins TEM foils will be prepared with a FIB technique using Hitachi NB5000. TEM will be performed using a Hitachi H-9500 high resolution transmission electron microscope at 300 kV.

4.2.2 Adiabatic Shear Bands

Adiabatic shear band – ASBs limit the nucleation and growth of nano-twins and because of that the materials starts to work soften and eventually fail. At each strain-rate the nano-twinning suppressing effect of ASBs are limited to a specific area around them that can be defined by an effective radius. Dynamic tensile experiments at dynamic strain rates will be performed on both HEAs using a modified split-Hopkinson pressure bar. To study the nano-twins and ASB deformation mechanisms and find the ASB effective radius for CoCrFeNi and CoCrFeMnNi HEAs, TEM foils will be prepared with a focused ion beam (FIB) technique using Hitachi NB5000. TEM will be performed using a Hitachi H-9500 high resolution transmission electron microscope at 300 kV on specimens deformed at strain-rates of 400 and 3000 s^{-1}.

4.2.3 Physics-Based Model

A physics-based molecular dynamics (MD) model using embedded-atom method potential and considering the adiabatic temperature rise and ASB will be developed. For the MD modeling LAMMPS (Large-scale Atomic/Molecular Massively Parallel Simulator) code and Palmetto cluster super computer will be used. The model then will be validated using the mechanical testing and electron microscopy results and compared to a modified Cook-Johnson (or Zerilli-Armstrong) constitutive equation.

Preliminary MD modeling has been conducted using the Fe-Cr-Ni interatomic potential developed by Bonny et al. [45]. This potential has been used because the potential for the HEAs under study has not been developed yet and Fe-Cr-Ni potential has been chosen as the closest available potential. It is of interest to find out how valid this potential is to be used as the HEAs potential. Figure 21 shows the deformed crystal of Fe-Ce-Ni atoms after undergoing a tensile experiment at 10k to the strain of 10%. Ovito visualization software has been used to visualize the results from from the modeling.
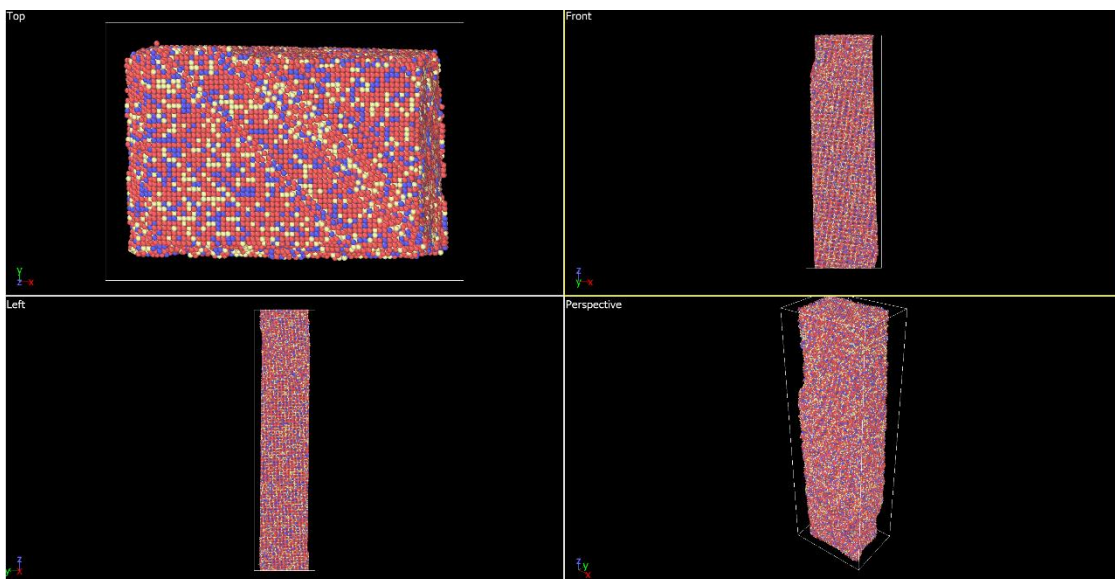

Figure 21: MD modeling results for Fe-Cr-Ni at 10k up to the strain of 10%.

Chapter 5. References

1.   Licavoli JJ, Gao MC, Sears JS, et al (2015) Microstructure and Mechanical Behavior of High-Entropy Alloys. J Mater Eng Perform. doi: 10.1007/s11665-015-1679-7

2.   Holcomb GR, Tylczak J, Carney C (2015) Oxidation of CoCrFeMnNi High Entropy Alloys. JOM. doi: 10.1007/s11837-015-1517-2

3.   Kumar N, Ying Q, Nie X, et al (2015) High strain-rate compressive deformation behavior of the Al0.1CrFeCoNi high entropy alloy. Mater Des 86:598–602 . doi: 10.1016/j.matdes.2015.07.161

4.   Yeh JW, Chen SK, Lin SJ, et al (2004) Nanostructured high-entropy alloys with multiple principal elements: Novel alloy design concepts and outcomes. Adv Eng Mater. doi: 10.1002/adem.200300567

5.   Cantor B, Chang ITH, Knight P, Vincent AJB (2004) Microstructural development in equiatomic multicomponent alloys. Mater Sci Eng A. doi: 10.1016/j.msea.2003.10.257

6.   Pickering EJ, Jones NG (2016) High-entropy alloys: a critical assessment of their founding principles and future prospects. Int Mater Rev. doi: 10.1080/09506608.2016.1180020

7.   Miracle DB (2017) High-Entropy Alloys: A Current Evaluation of Founding Ideas and Core Effects and Exploring "Nonlinear Alloys." JOM

8.   Huo W, Zhou H, Fang F, et al (2017) Strain-rate effect upon the tensile behavior of CoCrFeNi high-entropy alloys. Mater Sci Eng A. doi: 10.1016/j.msea.2017.02.077

9.   Gludovatz B, Hohenwarter A, Catoor D, et al (2014) A fracture-resistant high-entropy alloy for cryogenic applications. Science (80-). doi: 10.1126/science.1254581

10.   Diao HY, Feng R, Dahmen KA, Liaw PK (2017) Fundamental deformation behavior in high-entropy

alloys: An overview. Curr. Opin. Solid State Mater. Sci.

11. Wang S (2013) Atomic structure modeling of multi-principal-element alloys by the principle of maximum entropy. Entropy. doi: 10.3390/e15125536

12. Hemphill MA, Yuan T, Wang GY, et al (2012) Fatigue behavior of Al0.5CoCrCuFeNi high entropy alloys. Acta Mater. doi: 10.1016/j.actamat.2012.06.046

13. Otto F, Dlouhý A, Somsen C, et al (2013) The influences of temperature and microstructure on the tensile properties of a CoCrFeMnNi high-entropy alloy. Acta Mater. doi: 10.1016/j.actamat.2013.06.018

14. Gali A, George EP (2013) Tensile properties of high- and medium-entropy alloys. Intermetallics. doi: 10.1016/j.intermet.2013.03.018

15. Otto F, Yang Y, Bei H, George EP (2013) Relative effects of enthalpy and entropy on the phase stability of equiatomic high-entropy alloys. Acta Mater. doi: 10.1016/j.actamat.2013.01.042

16. Jones NG, Aveson JW, Bhowmik A, et al (2014) On the entropic stabilisation of an Al0.5CrFeCoNiCu high entropy alloy. Intermetallics. doi: 10.1016/j.intermet.2014.06.004

17. Jablonski PD, Licavoli JJ, Gao MC, Hawk JA (2015) Manufacturing of High Entropy Alloys. JOM. doi: 10.1007/s11837-015-1540-3

18. Patriarca L, Ojha A, Sehitoglu H, Chumlyakov YI (2016) Slip nucleation in single crystal FeNiCoCrMn high entropy alloy. Scr Mater. doi: 10.1016/j.scriptamat.2015.09.009

19. Abuzaid W, Sehitoglu H (2017) Critical resolved shear stress for slip and twin nucleation in single crystalline FeNiCoCrMn high entropy alloy. Mater Charact. doi: 10.1016/j.matchar.2017.05.014

20. Zhang ZZ, Mao MM, Wang J, et al (2015) Nanoscale origins of the damage tolerance of the high-

entropy alloy CrMnFeCoNi. Nat Commun 6:10143 . doi: 10.1038/ncomms10143

21. Laplanche G, Kostka A, Horst OM, et al (2016) Microstructure evolution and critical stress for twinning in the CrMnFeCoNi high-entropy alloy. Acta Mater. doi: 10.1016/j.actamat.2016.07.038

22. Lee SY, Lee SI, Hwang B (2018) Effect of strain rate on tensile and serration behaviors of an austenitic Fe-22Mn-0.7C twinning-induced plasticity steel. Mater Sci Eng A. doi: 10.1016/j.msea.2017.10.074

23. Barbier D, Gey N, Allain S, et al (2009) Analysis of the tensile behavior of a TWIP steel based on the texture and microstructure evolutions. Mater Sci Eng A. doi: 10.1016/j.msea.2008.09.031

24. Bouaziz O, Allain S, Scott CP, et al (2011) High manganese austenitic twinning induced plasticity steels: A review of the microstructure properties relationships. Curr. Opin. Solid State Mater. Sci.

25. Steinmetz DR, Jäpel T, Wietbrock B, et al (2013) Revealing the strain-hardening behavior of twinning-induced plasticity steels: Theory, simulations, experiments. Acta Mater. doi: 10.1016/j.actamat.2012.09.064

26. Karaman I, Sehitoglu H, Gall K, et al (2000) Deformation of single crystal hadfield steel by twinning and slip. Acta Mater. doi: 10.1016/S1359-6454(99)00383-3

27. Wang B, Fu A, Huang X, et al (2016) Mechanical Properties and Microstructure of the CoCrFeMnNi High Entropy Alloy Under High Strain Rate Compression. J Mater Eng Perform 25:2985–2992 . doi: 10.1007/s11665-016-2105-5

28. Sutton MA, Orteu JJ, Schreier HW (2009) Image correlation for shape, motion and deformation measurements. Springer

29. Pataky GJ, Sehitoglu H (2015) Experimental Methodology for Studying Strain Heterogeneity with

Microstructural Data from High Temperature Deformation. Exp Mech. doi: 10.1007/s11340-014-9926-7

30. Park JM, Moon J, Bae JW, et al (2018) Strain rate effects of dynamic compressive deformation on mechanical properties and microstructure of CoCrFeMnNi high-entropy alloy. Mater Sci Eng A. doi: 10.1016/j.msea.2018.02.031

31. Moon J, Qi Y, Tabachnikova E, et al (2018) Microstructure and Mechanical Properties of High-Entropy Alloy Co20Cr26Fe20Mn20Ni14 Processed by High-Pressure Torsion at 77 K and 300 K. Sci Rep 8:11074 . doi: 10.1038/s41598-018-29446-y

32. Dieter GE, Bacon D, Copley SM, et al (1988) Mechanical Metallurgy

33. Callister W, Rethwisch D (2007) Materials science and engineering: an introduction

34. Borchardt-Ott W (2012) Crystallography

35. Zener C, Hollomon JH (1944) Effect of strain rate upon plastic flow of steel. J Appl Phys. doi: 10.1063/1.1707363

36. Meyers M a. (1994) Dynamic Behavior of Materials. Dyn Behav Mater. doi: 10.1007/s11340-012-9598-0

37. Laplanche G, Kostka A, Reinhart C, et al (2017) Reasons for the superior mechanical properties of medium-entropy CrCoNi compared to high-entropy CrMnFeCoNi. Acta Mater. doi: 10.1016/j.actamat.2017.02.036

38. Zhang Y, Zhou YJ, Lin JP, et al (2008) Solid-solution phase formation rules for multi-component alloys. Adv Eng Mater. doi: 10.1002/adem.200700240

39. Yang X, Zhang Y (2012) Prediction of high-entropy stabilized solid-solution in multi-component

alloys. Mater Chem Phys. doi: 10.1016/j.matchemphys.2011.11.021

40.   Hertzberg RW (1996) Deformation and Fracture Mechanics of Engineering Materials

41.   Komarasamy M, Kumar N, Mishra RS, Liaw PK (2016) Anomalies in the deformation mechanism

        and kinetics of coarse-grained high entropy alloy. Mater Sci Eng A. doi:

        10.1016/j.msea.2015.12.063

42.   Moon J, Hong SI, Bae JW, et al (2017) On the strain rate-dependent deformation mechanism of

        CoCrFeMnNi high-entropy alloy at liquid nitrogen temperature. Mater Res Lett. doi:

        10.1080/21663831.2017.1323807

43.   Beyramali Kivy M, Asle Zaeem M (2017) Generalized stacking fault energies, ductilities, and

        twinnabilities of CoCrFeNi-based face-centered cubic high entropy alloys. Scr Mater. doi:

        10.1016/j.scriptamat.2017.06.014

44.   Wang Y, Liu B, Yan K, et al (2018) Probing deformation mechanisms of a FeCoCrNi high-entropy

        alloy at 293 and 77 K using in situ neutron diffraction. Acta Mater. doi:

        10.1016/J.ACTAMAT.2018.05.013

45.   Bonny G, Terentyev D, Pasianot RC, et al (2011) Interatomic potential to study plasticity in

        stainless steels: The FeNiCr model alloy. Model Simul Mater Sci Eng. doi: 10.1088/0965-

        0393/19/8/085008